Applied Clay Science 289 (2026) 108233

Contents lists available at ScienceDirect

Applied Clay Science

journal homepage: www.elsevier.com/locate/clay

Research Paper

Maximizing the reduction of vermiculite monolayers while concomitantly assuring colloidal stability of the obtained nematic suspensions

Xiong Xiong [a,1], Felix Uhlig [a,1], Ingmar Pietsch [a], Nashmiya Basheer [a], Sabine Rosenfeldt [b], Georg Papastavrou [c], Stefan Peiffer [d], Tillmann Lueders [e], Josef Breu [a,*]

[a] Bavarian Polymer Institute and Department of Chemistry, University of Bayreuth, Universitätsstr. 30, 95440 Bayreuth, Germany
[b] Physical Chemistry I, University of Bayreuth, Universitätsstr. 30, 95440 Bayreuth, Germany
[c] Physical Chemistry II – Interfaces and Nanoanalytics, University of Bayreuth, Universitätsstr. 30, 95440 Bayreuth, Germany
[d] Department of Hydrology, University of Bayreuth, Universitätsstr. 30, 95440 Bayreuth, Germany
[e] Chair of Ecological Microbiology, Bayreuth Center of Ecology and Environmental Research (BayCEER), University of Bayreuth, Dr-Hans-Frisch-Str. 1-3, 95448 Bayreuth, Germany

ARTICLE INFO

Keywords:
Vermiculite monolayers
Gas-barrier performance
Delamination
Reactive oxygen species

ABSTRACT

Vermiculite monolayers are typically two orders of magnitude larger than that of montmorillonite. The material therefore bears great potential for barrier improvement in polymer nanocomposites. Aside from the barrier improvement potential, vermiculite additionally holds promises for accelerating polymer degradation mitigating the microplastic issue. Structural iron will produce reactive oxygen species when submitted to natural anoxic/oxic cycles that have potential to render the surface more hydrophilic, and thus more attractive for colonization by fungi and bacteria. As a first step, here a concomitant optimization of vermiculite delamination, the colloidal stability of the resulting suspensions, and the extent of structural iron reduction, ultimately linked to reactive oxygen species generation, is presented. Delamination of vermiculite by one-dimensional dissolution produced monolayers with a huge aspect ratio of 9000 on average. Delamination, moreover, allows for a substantial increase in reduction with an ascorbate buffer as compared to stacked vermiculite tactoids. While for pristine or restacked Mg- and Na-vermiculite tactoids the reduction level was limited to 28%, the delaminated Li-vermiculite could be reduced to 44% of the total structural iron. This substantial difference is interpreted as indication that electron injections through the edges for delaminated types may be supplemented by injections through the basal planes of delaminated vermiculite.

1. Introduction

Vermiculite (VMT) is an abundant, affordable, natural layered silicate. VMT originates from parent minerals, typically biotite or phlogopite mica (Barshad, 1948). In some cases, VMT appears as large pseudomorphs of the parent mica crystals (Deer et al., 2013). As the formation of mica minerals is primarily associated with metamorphic and igneous processes, often involving intense heat and pressure deep within the Earth's crust, micas and its pseudomorphic derivatives, VMTs, come in large, mm-sized flakes. Structural iron is oxidized during the transformation to VMT, leading to a substantial reduction of charge density, while at the same time, the potassium interlayer cations are replaced by magnesium (Barshad and Kishk, 1968). The high hydration enthalpy of the latter yields hydrated interlayers in ambient humid conditions, and thus the interlayer is accessible for alterations like ion exchange (Dudko et al., 2022).

Although the pseudomorphs are rather metacrystals, and diameters of fundamental layers are much smaller than the pseudomorphs, upon utter delamination of VMTs into monolayers (Dudko et al., 2022), monolayers may be obtained with aspect ratios that are typically two orders of magnitude larger than that of montmorillonite, which is the most popular layered silicate filler for polymer nanocomposites used for improving barrier (Dudko et al., 2022). As according to Cussler permeability scales with the square of the aspect ratio, the potential for barrier improvement of vermiculite is 10,000 times that of a typical montmorillonite (Chen et al., 2019; Falla et al., 1996; Moggridge et al.,

* Corresponding author.
E-mail address: Josef.breu@uni-bayreuth.de (J. Breu).
[1] Contributed equally to this work.

https://doi.org/10.1016/j.clay.2026.108233
Received 22 December 2025; Received in revised form 9 April 2026; Accepted 9 April 2026
Available online 17 April 2026

2003). Barrier improvement is particularly sought after for biodegradable polymers as they show comparatively high permeabilities. InMat has patented barrier coating compositions containing dispersed, exfoliated (not delaminated!) vermiculite platelets (MicroLite, typical aspect ratio > 400) (Feeney et al., 2005). The comparatively low aspect ratio of 400 is due to incomplete delamination.

Aside from the thrilling barrier improvement potential, VMT additionally holds promises for accelerated (bio-)degradation of polymers in environmental compartments: Iron-bearing 2:1 layered silicates (clay minerals) have long been known to act as electron sources and sinks in the environment (‘geobatteries`) (Byrne et al., 2015; Yang et al., 2021). When the minerals are exposed to anoxic environments, for instance by flooding, structural Fe^{III} is used as a sink for electrons from bacterial respiration (Pentráková et al., 2013). After being re-exposed to oxygen in a subsequent oxic cycle, reactive oxygen species (ROS) such as superoxide radicals ($\bullet O_2$) and hydroxyl radicals ($\bullet OH$) are produced (Stucki, 2011; Yu et al., 2024). In combination with the structural iron, a strongly oxidizing Fenton reagent is obtained, and ROS produced in such a way have been identified as potent oxidants capable of degrading even persistent pollutants such as phenolic or halogenated (Babuponnusami and Muthukumar, 2014; Lin et al., 2025; Shokri and Fard, 2022). As ROS can also cause oxidative cleavage of carbon-carbon bonds in polymers (Celina, 2013), VMTs may not only improve the barrier properties of (bio-)degradable polymers but also accelerate their (bio-)degradation through surface alteration (chemical aging) of microplastic particles (Sajiki and Yonekubo, 2003). The introduction of polar functional groups has, for instance, been shown to accelerate fragmentation; reduction of molecular weight; and hydrophilization of polystyrene (Meides et al., 2021). Degradation of biodegradable polyesters is substantially hampered by their hydrophobic nature that requires eco-corona formation to allow enzymatic mineralization into carbon dioxide and water to become efficient (Guebitz and Cavaco-Paulo, 2008; Zhu et al., 2016). In this line, it has been shown that hydrophilization via oxidation of redox sensitive sulfur functionalities built into polyesters substantially accelerates ester hydrolysis (Fulajtar and Agarwal, 2024).

In this paper, natural VMT is aimed to be optimized as a barrier additive, which implies maximizing the degree of reduction of structural Fe, and hence its ROS generation potential, while delamination via one-dimensional (1D) dissolution into strict monolayers is concomitantly assured to obtain monolayers with maximum aspect ratio. Moreover, by comparing achievable reduction levels of stacked and delaminated vermiculite materials, valuable insight into the mechanism of electron injection may be obtained.

Iron in VMT normally occupies six-coordinate sites in the octahedral sheet of the silicate layer (Fig. 1a). Due to the distinct genesis and contrary to natural smectites like montmorillonite or nontronites, accessory Fe-oxyhydroxides may be neglected in respect to the redox behaviour of VMTs. The mechanisms for structural Fe^{III} reduction in 2:1 layered silicates, in particular the specific pathways by which the electrons are injected and penetrate the anisotropic layered structure, are poorly under-stood. The exact mechanism for electron injection into the platy silicate particles has been discussed controversially for decades in literature. In particular, whether electron injection can occur through both basal and edge surfaces is under debate (Gorski et al., 2012a; Gorski et al., 2012b; Gorski et al., 2013; Neumann et al., 2013). This might at least in part be related to the patchy nature of the silicate tactoids: Cationic reducing agents will preferentially adsorb at external basal surfaces or intercalate by strong electrostatic attraction,(Sposito et al., 1999; van Olphen, 1965) but complexing reductants like catechol will covalently link to edge sites by coordination of structural Fe^{III} (Fig. 1a) (Gorski et al., 2012a; Gorski et al., 2012b; Gorski et al., 2013; Neumann et al., 2013).

By comparing delaminated VMTs with various non-delaminated materials aside of materials aspects allows us to systematically modify the external surface area and the ratio of edge to basal surfaces. This delivers valuable insights into the mechanism of redox-chemistry.

2. Materials and methods

2.1. Materials

The VMT was purchased from a German importer, Isola, and originates from a mine in Afrika (IV-DB-DEU-Uganda-Namekara-2022-V2.pdf). According to the composition provided by the supplier the structural formula of a half unit cell is $[Mg_{0.37}]^{inter}[Mg_{2.44}Fe_{0.46}]^{oct}[Si_{3.15}Al_{0.85}]^{tet}O_{10}(OH)_2$. The cation exchange capacity as measured photometrically via $[Co(en)]^{3+}$ exchange was found to be 186 meq/100 g. Natural VMT flakes were first ground and sieved to sizes <100 μm size. All other chemicals used were supplied by Sigma Aldrich (LiCl (≥ 99%), butylamine (≥ 99.5%), sodium citrate dihydrate (≥ 99%), L-ascorbic acid (≥ 99%), citric acid (≥ 99%).

2.2. Cation exchange and delamination

The ground VMT was suspended in 100 mL of a 2 M (corresponds to 400 times the CEC) solution of the butylamine (C4) titrated by citric acid to pH 7 and then refluxed for 24 h. The high ionic strength prevents delamination at this stage. After five rounds of washing followed by centrifugation with a 50/50 vol% water/ethanol mixture (again the ethanol content prevents spontaneous delamination), the VMT was dried at 70 °C in a vacuum oven. Completeness of C4 exchange was confirmed by a rational 00 l series with a small coefficient of variation (CV) of 0.13%.

0.5 g of dry C4-vermiculite (C4VMT) is suspended in 100 mL deionized water whereupon delamination via 1D dissolution produces a 0.5 wt% nematic suspension (Walker, 1960). Specifically, 0.5 g of dry C4-vermiculite (C4VMT) was suspended in 100 mL of deionized water (0.5 wt%). The suspension was mixed by overhead stirring at 45 rpm for

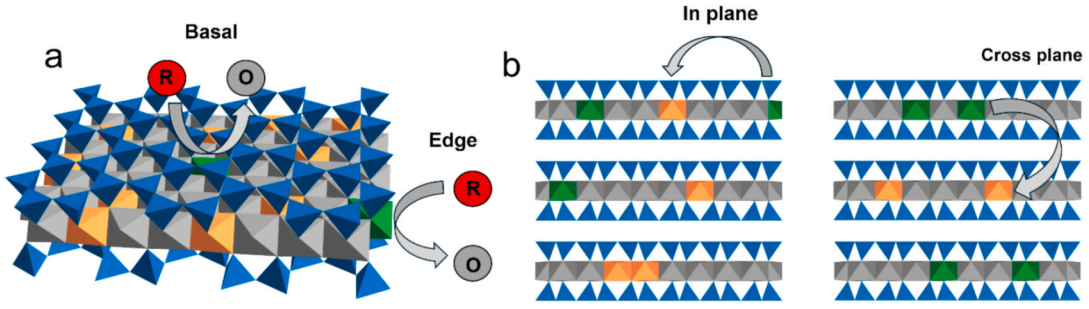

Fig. 1. Structure of a 2:1 layered silicate; green and orange octahedra represent Fe^{II} and Fe^{III} sites, respectively. Red dots (R) represent reductant and grey dots (O) represent oxidation product. Reduction of structural Fe^{III} is charge-balanced by incorporating additional cations in the interlayer. (a) Basal surfaces and edges represent distinct potential sites of electron injection. (b) In plane and cross plane electron hopping. (For interpretation of the references to colour in this figure legend, the reader is referred to the web version of this article.)

24 h at room temperature, during which delamination via one-dimensional dissolution yielded a nematic monolayer suspension. Delamination was considered complete when the dispersion showed persistent birefringence under crossed polarizers and no visible sedimentation over 24 h. Coarse residues were removed by centrifugation at 2500 rpm for 10 min, and the supernatant was used for further characterization. Li-vermiculite (LiVMT) was obtained by cation exchange by adding 100 mL LiCl (2 M, pH = 9 by adding LiOH) into the C4VMT suspension and stirring for 24 h at 70 °C. To assure a complete monoionic LiVMT, this ion exchange was repeated 3 times followed by washing as described above to reduce the ionic strength and finally dried in a vacuum oven at 80 °C. When suspending LiVMT in deionized water it spontaneously delaminates to a lamellar liquid crystalline nematic suspension. Delamination is complete within 24 h in an overhead shaker at room temperature (RT) and a birefringent suspension is obtained.

Na-vermiculite (NaVMT) is obtained following the procedure for LiVMT and using 100 mL NaOH (2 M). Contrary to LiVMT, when immersing NaVMT in deionized water it does not delaminate. Swelling is rather limited to crystalline swelling (van Olphen, 1965).

2.3. Chemical reduction

The various vermiculite samples were suspended in 20 mL de-oxygenated, Ar-saturated water (2 wt%, corresponding to 0.56 mmol structural Fe. To this suspension, 20 mL of a 100 mM ascorbate solution was added, giving a final volume of 40 mL with an ascorbate concentration of 50 mM corresponding to 2.0 mmol ascorbate in the suspension. Thus ascorbate is applied in a ~ 3.6-fold molar excess relative to structural Fe (ascorbate:Fe ≈ 3.6:1). The suspensions of reduced Li-vermiculites (R-LiVMT) were hold at 40 °C for up to 6 days and the reduction level was monitored with time by Mößbauer spectroscopy in Section 2.11. For pH-dependent reductions with LiVMT, the pH was adjusted between 4 and 10 with LiOH while maintaining the final ascorbate concentration at 50 mM.

2.4. X-ray diffraction

Cu K_α radiation ($\lambda = 1.5419$ Å) was used to collect XRD data using a Bragg–Brentano-type diffractometer (Empyrean, Malvern Panalytical BV, The Netherlands) fitted with a PIXcel-1D detector. Measurements were performed at 40 kV and 40 mA on oriented films in continuous scan mode over $2\theta = 1.0004$–$45.0000°$, using an angular step of 0.0131° and a time per step of 59.925 s (net time per step 58.395 s), corresponding to a scan speed of $0.0559° s^{-1}$ ($\approx 3.35° min^{-1}$).The HighScore Plus program from Malvern Panalytical was used for peak search.

2.5. Small angle X-ray scattering

A "Double Ganesha AIR" (SAXSLAB/Xenocs) was used to record small angle X-ray scattering (SAXS) data. This lab-based system uses a rotating copper anode (MicroMax-007 HF, Rigaku Corporation, Japan) to produce a focused X-ray beam and a position-sensitive detector (PILATUS 300 K, Dectris). The scattering vector range $q = 0.0024$–1.05 A^{-1} was covered. The VMT suspensions were added into 1 mm glass capillaries (Hilgenberg, code 4007610) for measuring. The data were circularly averaged and adjusted to account for the measurement duration, sample thickness, and incident beam. For background subtraction, a capillary filled with solvent was measured. Scatter (version 2.5) was used for further examination (Förster et al., 2010).

2.6. Static light scattering

A HORIBA LA-950 SLS device was used to record the particle size distribution of aqueous dispersions by static light scattering (SLS). The solid phase's refractive index was assumed to be 1.5.

2.7. Scanning electron microscopy

A ZEISS LEO 1530 (Carl Zeiss AG, Germany) operating at 3 kV was used to take scanning electron microscopy (SEM) images allowing to measure diameters of a larger assembly of individual monolayers spread on Si wafer.

2.8. Atomic force microscopy

Atomic force microscopy (AFM) measurements applying a Nanoscope Dimension 3100 (Bruker, formerly: Digital Instruments) in tapping mode has been applied to verify the aspect ratio of a single VMT monolayer. As cantilever model the OTESPA-R3 (Bruker) was used, which has a resonance frequency of 300 kHz and a typical spring constant of 26 N m^{-1}. Brukers NanoScope Analysis Vers. 1.80 software was used to process the AFM pictures. A first-order polynomial back-ground was subtracted from the topography using a threshold. Platelet heights were calculated using the NanoScope Analysis software's `step tool'. A few drops of a diluted solution (0.02 g L^{-1}) were slowly evaporated on a Si-wafer to obtain a sample with separated individual monolayers.

2.9. Inductively coupled plasma optical emission spectroscopy

The Fe content in the VMT samples was determined using Inductively Coupled Plasma Optical Emission Spectroscopy (ICP-OES) (Model: Bruker Aurora M90, Bruker Corporation). Prior to analysis, approximately 50 mg of the dried and finely ground VMT sample was digested using a CEM MARS 6 microwave digestion system with a mixture of hydrochloric acid (HCl) and nitric acid (HNO_3) (aqua regia) in a 4:1 (*v*/v) ratio. The digestion was performed at 180 °C for 30 min to ensure complete dissolution of the sample matrix. After cooling, the digested solution was filtered through a 0.45 μm membrane filter and diluted to a final volume of 50 mL with ultrapure deionized water. ICP-OES measurements were carried out under optimized conditions, using the Fe spectral line ($\lambda = 238.204$ nm) as the primary emission wavelength for Fe quantification. Calibration curves were prepared using a certified Fe standard solution at multiple concentrations. Each sample was measured in triplicate resulting in an average Fe content of 7.80 wt %. The typical standard deviation of the method is $\leq \pm 0.02$ wt%.

2.10. Electrophoretic mobility

For electrophoretic mobility measurements, aqueous dispersions with ca. 0.5 wt% of LiVMT and reduced LiVMT (R-LiVMT) were used. In general, for the investigation of the pH dependency of monolayers, a pH range from 4 to 10 was chosen, adjusted by either HCl or LiOH, to avoid any other cations interfering with the colloidal stability of delaminated monolayers. While the ionic strength was kept at 10 mM by LiCl in all cases. The pH was kept constant at 7 for the investigation of ionic sensitivity of monolayer suspensions. The homogenized suspension was measured immediately after immersion in the cell using a commercial microelectrophoresis device (ZetaView PMX 100, ParticleMetrix GmbH). Measurement data were collected at the stationary planes at least three times.

Zeta potentials (ζ) were calculated using the Smoluchowski equation:

$$\mu = \frac{\varepsilon \varepsilon_0 \zeta}{\eta}$$

where μ is the electrophoretic mobility, ε is the relative permittivity of the solvent, ε_0 is the permittivity of vacuum, and η is the dynamic viscosity of the solvent. When $\kappa R > 100$, the Smoluchowski limit is reached. This limit can still be used approximately when lamellated monolayers are used in place of spherical particles, as long as the platelets' aspect ratio is sufficiently large, and the electrolyte solution's ionic strength is

sufficiently high (Khoruzhenko et al., 2021). The reported zeta potential values were the average of 3 measurements (error: ±5 mV).

2.11. Möβbauer spectroscopy

The evolution of reduction was followed by taking approximately 20 mL of suspension at chosen time steps. The aliquots were washed with deionized, de-oxygenated and Ar-saturated water and centrifuged in inert atmosphere in a glovebox. Some 0.20 g of powder was packed in the glovebox into a circular sample holder. Samples were sealed with Kapton film to mitigate re-oxidation and were immediately measured.

Mößbauer spectra were collected with a configuration designed for high-resolution measurements. The setup consisted of a WissEl Mößbauer Drive System MR-360, an MA-260 velocity transducer for precise and controlled motion of the ^{57}Co(Rh) source (activity: ~50 mCi), and a KETEK silicon drift detector AXAS-M. The gain and shaping time constants were optimized experimentally. Data was collected using a CMCA-550 module in MCS [WINDOW] mode, enabling the selective detection of the 14.4 keV Mößbauer line. Calibration was carried out using a ^{57}Fe-enriched metallic foil. Measurements were taken at room temperature. The sinusoidal velocity waveform for the source motion was generated by a DFG-1000 digital function generator, which was synchronized with the CMCA-550 channel sweep. (Spectral data were processed and analysed with MossA software to ensure accurate alignment and energy calibration (Prescher et al., 2012).

3. Results and discussion

3.1. Delamination of VMT into monolayers by 1D dissolution

By far most frequently, an increase of aspect ratios of layered materials is attempted by mechanical exfoliation, as for instance applied for the exfoliated VMT produced by MicroLite. (www.specialtyvermiculite.com/products/microlite) This is a brute force approach as it is applied in a cohesive state, meaning that adjacent individual layers in the crystal stack (labelled tactoids instead of crystal because of disorder in the stacking direction) attract each other by Coulombic forces, hydrogen bonding, and van der Waals interactions. With liquid phase exfoliation, the yields are usually mediocre, a broad distribution of thicknesses is obtained, and as particles are frequently broken instead of being solely thinned by shearing, the aspect ratio inherent to the diameter of the parent layers is not reached by far.

Setting the conditions right for ionic layered compounds like layered silicates, a spontaneous, thermodynamically driven delamination into monolayers may be realized (Daab et al., 2017; Dudko et al., 2022). Much like the dissolution of simple salts, but restricted to the stacking direction, infinite separation of individual monolayers by repulsion is observed. Basically, once the interlayer height is increased beyond a certain threshold, the entropy of interlayer entities overcomes the attraction of anionic layers and interlayer cations (Dudko et al., 2022). For this to happen, interlayer cations must segregate to the Helmholtz layers on both sides of the interlayer space. This only works for monovalent cations. Divalent cations rather reside in the middle of the interlayer, and thus block delamination. For low charge densities of the anionic layers, like with smectites like hectorite in combination with cations offering sufficient hydration enthalpy like Na^+, hydration of interlayer cations is sufficient to take the system over the threshold (Daab et al., 2018b). With higher charge densities like with VMTs, bulky yet hydrophilic organocations are needed to open the interlayer space beyond the threshold separation by exerting steric stress (Daab et al., 2018a). As this 1D dissolution process is gentle, requiring simply overhead shaking, the intrinsic aspect ratio of the pristine platelet diameter is preserved (Dudko et al., 2022). Because the monolayers that have been delaminated have large diameters, the suspensions that are obtained are usually not isotropic but represent lamellar liquid crystals (nematic phases). Monolayers of 10 μm diameter would have to be separated to more than 10 μm before rotation is no longer hindered. To get isotropic suspensions with 2:1 silicate monolayers that are 1 nm thin, these suspension would have to be diluted to 10^{-2} vol%.

3.2. Complete ion exchange of pristine Mg-vermiculite

The pristine Mg-vermiculite (MgVMT) is incapable of spontaneous delamination for two reasons. Firstly, the charge density of VMT is too high to overcome the threshold separation just because of the hydration forces of the interlayer cation. Secondly, as a divalent cation, Mg^{2+} will reside in the middle of the interlayer, evenly interacting with both adjacent silicate layers and therefore blocking delamination. Thus, Mg^{2+} must be completely exchanged by a bulky organocation of higher selectivity for the interlayer space. As suggested by Walker, we choose butylammonium was chosen (Walker, 1960). Unfortunately, the selectivity of Mg^{2+} for the interlayer site is still too high to achieve a complete ion exchange. Walker first had to obtain monoionic NaVMT by changing the exchange solution weekly over a period of more than a year. In the second step, Na^+ could then be exchanged for butylammonium to trigger delamination into a gel. The equilibrium of the Mg^{2+} exchange, however, may easily be shifted substantially by complexation with citrate (Dudko et al., 2022). Applying butylammonium citrate allowed a complete ion exchange by refluxing the MgVMT for one day. When reducing the ionic strength after ion exchange to levels below 0.05 M by repeated washing followed by centrifugation, the organo-VMT spontaneously delaminated (Dudko et al., 2022). As we next wanted to optimize the reduction of structural iron, we were aiming to compare monoionic VMT with inorganic cations (Mg^{2+}, Na^+, Li^+). As the reduction of structural iron was next to be optimized, monoionic VMT with inorganic cations (Mg^{2+}, Na^+, Li^+) was compared. For this, butylammonium can easily be replaced quantitatively by deprotonation with NaOH or LiOH, respectively.

3.3. Characterization of delaminated LiVMT monolayers

Small angle scattering (SAXS, Fig. 2a) of fully delaminated nematic gels of VMT (5 vol%) show two characteristic features: First a q^{-2} slope indicating 2D objects scattering and second a *00 l* series indicating the repulsive separation to 15 nm (q = 0.042 Å^{-1}) of adjacent coplanar monolayers in the nematic gel. This separation is, of course defined by the concentration of the gel and increases with further dilution. The SAXS pattern was calculated using the model of 1D stacked discs (Fig. 2a red line) with a diameter of 9000 nm and a thickness of 1 nm. The diameter was taken in line with the average diameter of monolayers as determined by static light scattering (SLS, Fig. 2b). The monolayer nature of the monolayers was confirmed by atomic force microscopy (AFM, Fig. 2c). Since AFM images were recorded under ambient conditions, the hydrated counter cations (Li^+) attached to the then external basal surfaces will add to the observed thickness. A thickness of 1.5 nm indicates a monolayer of 1 nm thickness amended by the thickness of a hexahydrate cation (Loch et al., 2022; Mähler and Persson, 2012). The monolayer is irregularly shaped with a long extension of 6 μm that is in decent agreement with the distribution of hydrodynamic diameters observed in SLS. A third independent measure of the typical diameters was obtained by scanning electron microscopy (SEM, Fig. 2d) that gave a mean diameter of 22 monolayers of 9 μm. While the AFM image shown in Fig. 2c is typical and representative, AFM fails to present proof for complete delamination. This needs a bulk method as represented by SAXS. SAXS curves were recorded to a q value where restacked aggregates are expected. As within experimental detection limit no signal is observed for restacked tactoids this indicates complete delamination within experimental errors.

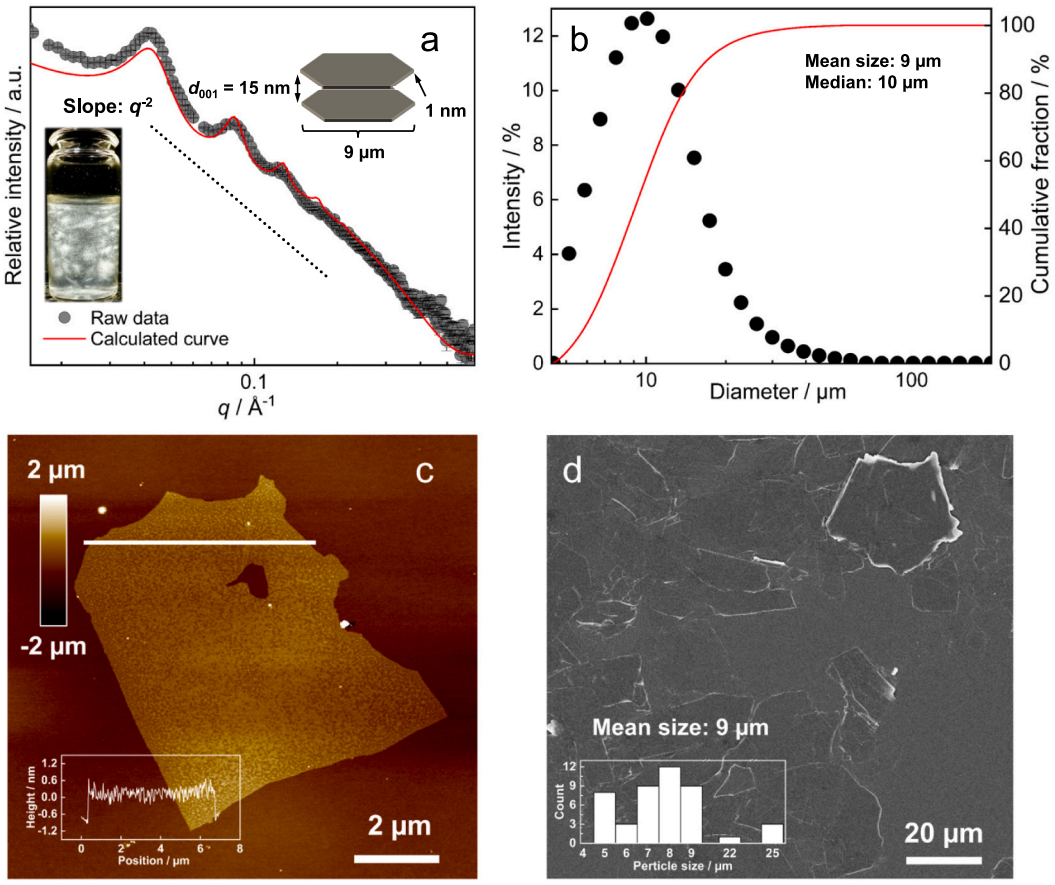

Fig. 2. Characterization of delaminated vermiculite (VMT) nanosheets and their nematic suspensions. (a) SAXS of the nematic phase. Inset: 1 wt% LiVMT suspension in water displaying birefringence under cross-polarized light. (b) Number weighted size distribution indicating a mean size of 9 µm as determined by SLS. (c) Topographic AFM image of a typical VMT monolayer. Inset: Height profile measured along the indicated line. (d) SEM image of VMT monolayers cast on a silicon wafer. Inset: Particle size distribution obtained from the SEM image, with a mean size of 9 µm.

3.4. Maximizing the reduction level for a delaminated nematic suspension of LiVMT

2:1 layered silicates are patchy particles with distinct surface functions of basal surfaces and edges. Basal surfaces are terminated by siloxane and alloxan groups. They are chemically inert and carry a permanent negative charge resulting from isomorphous substitutions. Edges represent extrinsic defects and are terminated by hydroxyl groups, which may be protonated or deprotonated depending on surrounding pH (Gao et al., 2023). Depending on the type of cations exposed, the point of zero charge may vary between pH 5 and 7, with VMTs located at the lower end because of the substantial content of trivalent octahedral cations. Cations residing at the edges of the octahedral layer may be coordinated by complexing ligands. Due to the platy morphology, the external surface area of VMT is, however, dominated by the basal surfaces. Given the large diameter of individual layers, edge surfaces may amount to less than 5% depending on the aspect ratio of the layered particle.

For many years, redox reactions via edge surfaces following coordination of reducing agents to structural Fe^{III} were the dominating, if not the only, reaction mechanism accepted (Fig. 1a) (Neumann et al., 2013; Pothanamkandathil et al., 2024; Rothwell et al., 2023; Schaefer et al., 2011). VMT layers are, however, electric insulators. In-plane electron shuttling from the surface to more remote structural Fe atoms in the same octahedral sheet (Fig. 1b, left) might therefore become the rate-determining or reduction limiting process. A polaron hopping conduction has been suggested (Maruvada et al., 2022). This hopping requires, however, a percolation path of mixed valent Fe^{II}— Fe^{III}—Fe^{II} configurations. The activation energy for hopping will be greatly influenced by the total Fe content, mixed valency, and the distribution pattern of Fe within the octahedral sheet (Latta et al., 2017; Rosso and Ilton, 2005). The Fe content of the VMT used in this study was 7.8 wt%. (1.4 mmol•g^{-1}). Approximately 1 out of 8 octahedral cations is Fe, amounting to typical minimum distances between two Fe sites within the same octahedral sheet (intralayer) of 5.2 Å and 6.0 Å when assuming a statistical substitution of Fe sites. Intralayer electron hopping, therefore, faces serious barriers (Sainz-Díaz et al., 2001).

The assumption of a statistical substitution of structural Fe might, of course, not be fully justified despite the high-temperature genesis history of VMTs and the high entropy involved favouring solid solutions (Palin et al., 2004; Sainz-Diaz et al., 2003). Applying Monte Carlo simulations, a general tendency of Fe to form clusters has been reported for octahedral sheets of natural clay minerals like illites and smectites (Ortega-Castro et al., 2010; Sainz-Díaz et al., 2003). Quite different segregation behaviours were observed for different Al:Fe:Mg ratios (Sainz-Diaz et al., 2003; Vantelon et al., 2003). The octahedral Fe clustering patterns might therefore be indeed a so-far-overlooked structural parameter that determines the redox properties of VMTs (Gorski et al., 2012a; Gorski et al., 2012b; Gorski et al., 2013; Pothanamkandathil et al., 2024).

In any case, the electric conductivity of VMTs and their parent mica ancestors is negligible, and they are regarded to be large bandgap electrical insulators due to their low Fe content (Maruvada et al., 2022). This is underlined by the fact that such micas are used for manufacturing mica tapes applied for high-voltage insulation systems (Krempel, Inc., 2023).

Alternatively, electrons might also be injected through external basal surfaces (Neumann et al., 2013). For samples that are not delaminated, the question arises for this case how electrons are shuttled from one to the next silicate layer towards the remote centre of the tactoids (Fig. 1b, right) once they have been injected through an external basal plane. Even if two Fe sites happen to be arranged above each other in the stacking direction, the distance across the hydrated interlayer corresponds to the *d*-spacing (14.2 Å for MgVMT at 75% r.h., Fig. S1) (Ruiz-Conde et al., 1996; Suzuki et al., 1987). By choosing the two non-delaminating interlayer cations of different hydration enthalpy ($E_{hyd.}$/val: 1000 and 400 kJ/mol for Mg^{2+} and Na^{+}, respectively) (Marcus, 1987, 1991), the interlayer Fe—Fe distances can be varied systematically to some extent, which in turn will give indirect information on the relative importance of the various electron migration paths. MgVMT adopts a two-water layer hydrate with a *d*-spacing with 14.2 Å, while NaVMT only is hydrated to the monolayer hydrate with 12.6 Å (Fig. S1). Li-VMT has been labelled superhydrophilic and is the only type of material that is fully delaminated into a nematic liquid crystalline suspension (Huang et al., 2020). This implies that with Mg- and NaVMT, reductants can only inject electrons through the external basal or edge surface (Neumann et al., 2013). Given a typical thickness of MgVMT tactoids of 50 μm, only 2 out of more than 30,000 basal surfaces will be in direct contact with the solution containing the reductant (Bergaya and Lagaly, 2013). Contrary to this, for delaminated LiVMT, all basal surfaces are in contact with the solution.

If indeed reduction through the basal surface would be a feasible pathway, the electron injection with 2:1 layered silicates is always an outer sphere process because octahedral Fe^{III} is separated by the tetrahedral sheets (~ 3 Å) from the surface. If reductants or mediators cannot replace the pristine redox-inert hydrated counter-cations like Li^{+} in the Helmholtz layer, octahedral cations will be insulated by another ~4 Å. Anionic reductants might further be hindered by electrostatic repulsion. As the Debye length shrinks with ionic strength, at higher values anionic reductants get closer to the basal surface at a higher concentration (Israelachvili, 2011). Nematic suspensions, however, are sensitive to ionic strength, and at values >0.05 M, the electrostatic repulsion between adjacent monolayers is no longer sufficient, thus, delaminated monolayer suspensions become unstable (Gabriel et al., 1996; Michot et al., 2006; Paineau et al., 2011).

Cationic reductants will at least partially be adsorbed in the inner Helmholtz layer and thus would get closer to the structural Fe sites (Hunter, 2013). As organocations in general have a higher selectivity for the Helmholtz layer (Bergaya and Lagaly, 2013), this in turn will alter the zeta potential and thus might affect the electrostatic stabilization of delaminated monolayers. Moreover, when a cationic reductant is oxidized during electron transfer, it will end up at least as a dication. Dications reverse 1D dissolution as they definitely trigger flocculation, and therefore any cationic reductants will not match with the delaminated state. Even strong neutral molecular reductants would end up after electron injection as organocations immobilized at the basal surface and hence, destabilize the colloidal suspensions (Lagaly, 2006).

As a reductant, therefore the ascorbic acid/Li-ascorbate buffer was chosen for chemical reduction (Hynes and Kelly, 1988; Manjanna, 2008). For structural iron of 2:1 layered silicates, a rather broad range of reduction potentials for structural Fe was reported (Gorski et al., 2012a; Gorski et al., 2012b; Pothanamkandathil et al., 2024), which recently has been attributed to the fact that chemical reduction involves a large driving force and in conjunction with usually applied relatively short equilibration times might lead to gradients in the Fe^{III}/Fe^{II} ratio. The redox potential vs. standard hydrogen electrode (E_h) of purified naturally occurring smectite SWa-1 montmorillonite (12.6 wt% Fe) was reported to be around −0.2 V, and the potential decreases with progressing reduction to −0.5 V at 90% reduction (Gorski et al., 2012b). The reduction potential of ascorbic acid is dependent on pH, and its reduction power should be sufficient at pH values above pH = 4. At pH = 9, the redox potential of ascorbate is as high as −0.472 (Bard, 2017; Wagner and Buettner, 2023). During reduction, a couple of parameters are highly correlated: For instance, with reduction, the charge density of the silicate layer increases. While this is compensated by intercalation or adsorption of additional cations from solution, most importantly, this might substantially modify the zeta potential (Manceau et al., 2000; Stucki, 2011).

The pH may be adjusted by the degree of neutralization of ascorbic acid, which in turn influences the ionic strength in solution and hence, the zeta (Hunter, 2013; Serrano-Lotina et al., 2023). As previously discussed, the zeta potential influences the proximity with which the anionic reductant can approach the basal surfaces.

Delaminated R-LiVMT suspensions are colloidally stable over the complete investigated pH range between 4 and 10 (Fig. 3a) as the zeta potential of R-LiVMT is substantially more negative (−63 mV to −52 mV) as compared to the oxidized LiVMT. This significant difference in surface potential with different charge density is in line with previous measurements of diffuse layer potentials based on colloidal probe techniques, and where it was found that $[Na_{0.5}]^{inter}[Mg_{2.5}Li_{0.5}]^{oct}[Si_4]^{tet}O_{10}F_2$ had a less negative potential than $[Na_{0.85}]^{inter}[Li_{0.85}Mg_{2.15}]^{oct}[Si_4]^{tet}O_{10}F_2$ (Kuznetsov et al., 2020). Please note, while it has been shown long ago that reduction increases the permanent negative charge of the silicate layers and hence the cation exchange capacity; for delaminated monolayers it is crucial to distinguish between the charge density of the layer and the zeta potential (surface charge seen from the surrounding medium) (Stucki, 2011). As the share of counter cations residing in the Helmholtz layer increases with charge density of the silicate layer, a higher charge density might even lead to a lower zeta potential.

It moreover implies that during reduction it becomes increasingly more difficult for the negative reductant to approach the basal surface. For R-LiVMT, the zeta potential does not change much with pH. Contrary to this, the zeta potential of the oxidized LiVMT decreases from −10 to −40 mV with increasing pH. As the nematic suspensions are solely electrostatically stabilized, with zeta potentials higher than −30 mV, reaggregation followed by sedimentation was observed. This implies, on the one hand, that reduction must take place at pH values above 6. On the other hand, with increasing pH, it will become increasingly more difficult for an anionic reductant to approach the basal surface. The degree of reduction achieved after 50 h nevertheless steadily increases (Fig. 3a blue dots) with pH, suggesting that the reduction power of the ascorbate is more important than the zeta potential for the maximum degree of reduction of the monolayer dispersion. From pH 7 to 9, the reduced Fe^{II} yield increased from 27.5% to 44.3%.

Taking the various parameter into consideration, pH = 9 was chosen for optimum reduction (Fig. 3a, blue dots). As the zeta potential and the stability of the delaminated VMT suspensions are also dependent on ionic strength, the maximum ionic strength tolerated was determined (Fig. 3b) by dosing LiCl to the nematic suspensions. Both, LiVMT and R-LiVMT, flocculate above 50 mM ionic strength, which limits the concentration of the reductant to 50 mM. This still corresponds to a 3.6-fold stoichiometric ratio of reductant to structural iron. This dependence on a critical ionic strength threshold—above which the stability of the VMT suspension rapidly decreases—is particularly interesting. According to the electrophoretic mobility theory developed by O'Brien and White (O'Brien and White, 1978), such non-monotonic dependencies (including mobility maxima) can arise from the complex interplay between electrostatic and hydrodynamic forces in the diffuse double layer surrounding colloidal particles, which may qualitatively explain the observed flocculation behaviour at elevated ionic strength.

3.5. Comparison of the reduction level of various VMT samples

Once the optimum reducing conditions (pH = 9, 50 mM in ascorbate) were set, the degree of reduction as a function of time was monitored by ^{57}Fe Mößbauer spectroscopy (Fig. 4). Four variations of VMT were tested that refer to the various structural parameters discussed and that are

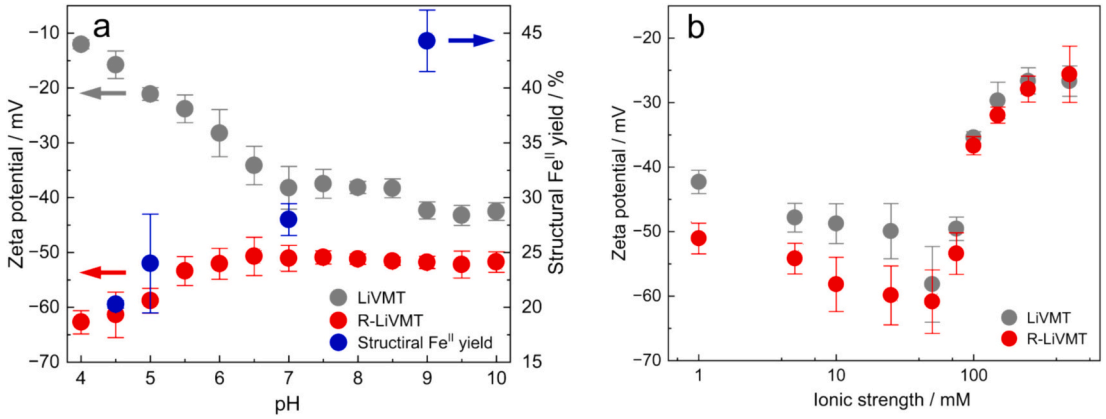

Fig. 3. Characterization of the colloidal behaviour of delaminated VMT monolayers before and after reduction. (a) Zeta potential of LiVMT (grey dots), reduced LiVMT (R-LiVMT, red dots) at 44.3% reduction, and structural Fe^{II} yield (blue dots) as a function of pH. The ionic background was kept at 10 mM for all samples. (b) Zeta potential of LiVMT (grey dots) and R-LiVMT (red dots) as a function of salinity, where the pH value is kept at 9 for both samples. (For interpretation of the references to colour in this figure legend, the reader is referred to the web version of this article.)

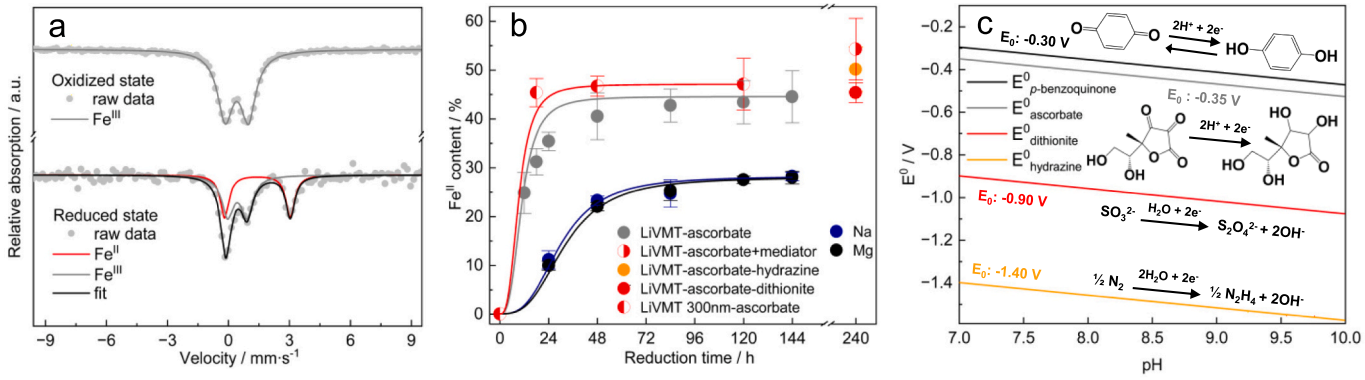

Fig. 4. Chemical reduction of various VMT types. (a) Mößbauer spectra of delaminated LiVMT before (top) and after (bottom) reduction by 50 mM ascorbate. (b) Structural Fe^{II} yield of LiVMT monolayers, chopped LiVMT (LiVMT, 300 nm), restacked NaVMT, and pristine MgVMT with reduction duration by ascorbate. The curves serve as guide to the eye. To the samples fully reduced with ascorbate, hydrazine, dithionite or redox mediator/ascorbate were added and the reduction levels obtained after another 120 h are included as isolated points. (c) pH dependency of reduction potentials of the various reductants applied.

thought to influence the reduction level: Comparing delaminated (LiVMT) with non-delaminated samples (NaVMT and pristine MgVMT) will indicate the importance of electron injection via accessible basal planes. Comparing MgVMT with NaVMT, both being stacked into tactoids, will indicate whether electron hopping from one silicate layer to the next across the different interlayer heights would have an influence. Finally, comparing LiVMT with the large pristine diameter of ~9 μm with the same sample that has been chopped up by ultrasonication to smaller diameters, typically 300 nm (LiVMT, 300 nm) will indicate the importance of intraplane electron hopping following electron injection. As the share of edge surfaces is substantially increased with the smaller LiVMT, 300 nm and as the length of the percolation path to the centre of the layer becomes substantially shorter, a faster kinetics is expected.

The Mößbauer spectrum of pristine LiVMT monolayers (Fig. 4a, top) before reduction shows that all structural Fe in LiVMT is present as octahedral Fe^{III}, no tetrahedral Fe^{III} was detected. Reaction of monolayers with 50 mM ascorbate at pH 9 resulted in an additional doublet in the Mößbauer spectrum (Fig. 4a, bottom), indicating the presence of an octahedral Fe^{II} doublet (red line, chemical shift (CS): 1.33 mm/s, quadrupole splitting (QS): 2.86 mm/s), which is within the expected range for structural Fe^{II} in layered (Dyar et al., 2006; Manceau et al., 2000; Murad, 2010). The Fe^{II} doublet comprises 44.3% of the spectral area, indicating that 44.3% of structural Fe in LiVMT monolayers were reduced (Table S1). The stacked tactoids with orders of magnitude less external basal surface (Fig. 4b) show a much lower maximum reduction degree. The substantial difference is a strong indication for electron injection through basal surfaces for delaminated LiVMT.

As both NaVMT (28%) and MgVMT (28%) reach the same reduction levels, electron transfer across the interlayer into the adjacent silicate layers seems to be irrelevant for the maximum reduction accessible as could have been triggered by the difference in basal spacing. The kinetics of reduction for non-delaminated VMTs are, moreover, much slower as compared to the delaminated LiVMT. The latter reaches the plateau of the maximum reduction level already after 50 h while the stacked tactoids need more than 120 h to reach a constant level. An induction period furthermore seems to be present for tactoids (NaVMT and MgVMT), which is hypothesized to be related to the initial formation of mixed valency that subsequently facilitates intralayer electron hopping. The substantially faster onset of reduction for LiVMT might suggest that injection of electrons from the basal plane contributes to the kinetics already at early stages of reduction.

To quantify reduction kinetics from ascorbate to a structural Fe^{III} or from structural Fe^{II} to the nearest structural Fe^{III}, Marcus theory could be applied based on first principle calculations (Adelstein et al., 2014; Wu and Van Voorhis, 2006). In the realm of clay minerals, Marcus theory has, however, only been applied to edge sites in the octahedral sheets, as organic reductants can coordinate to Fe-centers at a shorter distance (Gorski et al., 2013; Neumann et al., 2013; Pothanamkandathil et al., 2024; Rosso and Ilton, 2005). Even this approach has rarely been chosen, mostly because of its computational expense (Adelstein et al., 2014;

Wu and Van Voorhis, 2006). As this is beyond the scope of this paper, a qualitative discussion is provided in the following. Marcus theory primarily describes the kinetics of electron transfer reactions, providing a framework for calculating the associated rate constants and activation energies. According to Marcus theory, the electron transfer rate is determined by the free energy change (ΔG°), the reorganization energy (λ), and the electron coupling (H_{AB}) (Gray and Winkler, 2005; Marcus, 1993). The latter implies an exponential decrease of the rate with distance.

If kinetics and the degree of reduction are governed solely by edge injection followed by electron hopping within the octahedral sheet, no difference should be observed between delaminated (LiVMT, Fig. 4b) and stacked materials (NaVMT and MgVMT, Fig. 4b), which clearly is not the case. Bond distances between Fe at the edge and coordinated ascorbate ligands are in the range of 2.2 to 2.8 Å, and thus, injection will not be rate determining (Kontoghiorghes et al., 2020; Kwon et al., 2020). Rather, the intralayer hopping to the centre of the silicate layer with the shortest distances between two Fe centers of 5.2 Å and 6.0 Å will determine the rate (Rosso and Ilton, 2005). Although not clearly significant, the reduction rate of chopped 300 nm diameter material (LiVMT, 300 nm, Fig. 4b) seems to be slightly faster than for the large diameter LiVMT. This trend would also support the commonly accepted view of edge injection being the significant reduction pathway (Neumann et al., 2013).

As reduction with delaminated samples is faster and leads to substantially higher reduction levels, it is safe to assume that basal planes are playing a significant role during the reduction aside of edge injection (Neumann et al., 2013). In the delaminated state, all basal surfaces and edges are exposed to the reductant dissolved in the dispersion medium. The basal planes of the silicate layers are decorated by an immobile outer Helmholtz layer built by octahedral hexaaqua complexes (Hunter, 2013; Israelachvili, 2011). Its thickness may be estimated from the *d*-spacing found for the two-water layer hydrate, which for LiVMT is 14 Å (Suzuki et al., 1987). Subtracting 9.6 Å of the monolayer thickness of 2:1 layered silicates, a thickness of 4.4 Å may be derived for the Helmholtz layer. Anionic reductants cannot penetrate the Helmholtz layer.

Moreover, an insulating tetrahedral sheet between the Fe sites and the redox-active organic molecule outside the Helmholtz layer adds another ~4.8 Å (i.e., half of the monolayer thickness), resulting in a total minimum electron transfer distance of ~9.2 Å when injection occurs through basal planes. This value is approaching the effective limit of electron tunnelling. In well-studied systems such as thiol-based self-assembled monolayers (SAMs), electron transfer is found to decay exponentially with distance, becoming negligible beyond 1.5–2.0 nm (Chidsey, 1991; Eckermann et al., 2010). Similarly, scanning tunnelling microscopy measurements typically operate at tip–surface distances below 1 nm to ensure measurable current (Tersoff and Hamann, 1985). These comparisons demonstrate that although electron injection across 9.2 Å is still possible, it likely occurs with much lower efficiency than through edge sites, where the spatial separation between Fe centers and reductants can be significantly shorter.

Nevertheless, a significant amount of ascorbate is still able to approach the octahedral Fe from the basal planes to this distance. These estimated distances for basal plane injection are substantially longer than the distances involved for electron injection through edges followed by intralayer hopping. According to Markus theory, the shorter distance will be connected to faster kinetics, and this is why most studies assume this to be the dominant reduction path (Gray and Winkler, 2005; Marcus and Sutin, 1985). For highly oxidized VMTs like the one used here, at early states of reduction, only very few mixed valence Fe^{II}—Fe^{III}—Fe^{II} percolation paths are available for intralayer electron hopping into the centre of the layer. This might explain the induction period and the slower reduction progress for stacked variants (Gorski et al., 2012b; Gorski et al., 2013). With the progress of reduction, gradients or islands with fully reduced Fe^{II}—Fe^{II}—Fe^{II} clusters might evolve, and the reductions stop at a low level of <30%. Alternatively, for stacked variants, reduction might stop if Fe is not uniformly distributed and some of the structural Fe is not connected to percolation paths at all.

The substantially higher reduction levels and the faster reduction kinetics observed for delaminated LiVMT represent clear evidence that injection of electrons from the basal plane is possible. Moreover, electrons injected through basal planes instantly create a uniform level of mixed valence Fe^{II}—Fe^{III}—Fe^{II} configurations, which at the same time should speed up electron hopping throughout the silicate layer, mitigating gradient formation. For delaminated LiVMT, all basal planes are accessible to ascorbate penetrating the diffuse double layer, and ascorbate is applied in stoichiometric excess. Even Fe sites remote from Fe^{II}—Fe^{III}—Fe^{II} percolation paths may equally easy be reached from external basal planes.

The estimated ascorbate concentrations near the monolayer basal surfaces (Fig. S2) suggest only a minor decrease in concentration due to the negative surface potential. These values are derived from a continuum Poisson–Boltzmann approach and should therefore be interpreted as qualitative approximations (López-García et al., 2011). Note that ascorbate is a relatively large anion, and continuum models may not fully capture steric effects or specific ion–surface interactions. Furthermore, the immobile nature of the Helmholtz layer limits the physical access of reductants to the structural Fe sites (Hunter, 2013). Therefore, the distance of closest approach must be interpreted not as a penetration into the Helmholtz layer, but rather as a limiting proximity at which electrons might tunnel from the solvated reductant across the interfacial barrier. Given these constraints, Fig. S2 illustrates a theoretical concentration profile using the Gouy–Chapman model (López-García et al., 2011), but the actual interfacial reduction efficiency is more likely governed by the tunnelling distance and local percolation paths of Fe^{III} centres.

Contrary to the limited reduction observed even with delaminated LiVMT, for nanoscopic, high Fe-content nontronites, reduction levels of up to 91% have been reported (Manceau et al., 2000; Qian et al., 2023). Nontronites exhibit significant Fe − Fe clustering that might easily lead to in-plane percolation paths with short distances between Fe centres, allowing injected electrons to easily migrate within the octahedral sheet. SWa-1 montmorillonite with much lower Fe content can, however, also be reduced to levels >90% (Gorski et al., 2012b).

If the reduction level for LiVMT is limited to less than 50%, although all structural Fe atoms have the same distance to the basal surface and injection through the basal surface is feasible, this limit cannot be related to the kinetics of electron hopping within an octahedral sheet nor to Fe sites not included in percolation paths.

Three additional experiments were performed to probe potential causes for the reduction limit. First, a neutral redox mediator; second, a stronger anionic reductant; and third, a potent cationic reductant was applied (Fig. 4c).

p-Benzoquinone is a water-soluble neutral molecule frequently used as a redox mediator for clay minerals. It has a redox potential (E_0 = −0.42 V at pH 9, Fig. 4c, blue line) that falls somewhere between ascorbate and Fe^{III}/Fe^{II}. When this redox mediator, together with additional ascorbate, was added to the R-LiVMT, the reduction level only slightly increased to 55%, indicating that the negative charge of ascorbate is most likely not a limiting factor.

Next, the reducing power was increased by adding dithionate or hydrazine to R-LiVMT. At pH 9, ascorbate has a potential of −0.47 V, while dithionite and hydrazine have much higher reduction potentials of −1.01 V and − 1.52 V, respectively (Fig. 4c). Despite the higher reduction power, little additional structural Fe could be reduced (Fig. 4b). Specifically, the reduction of structural iron by hydrazine was increased by as little as 6% (Fig. 4b, orange dot), while with dithionite (Fig. 4b, red dot), no significant change was observed at all.

These additional experiments suggest that for VMTs approximately half of the structural Fe must have a much higher reduction potential as observed for other common 2:1 clay minerals. The reason for this can only be speculated on: In 2:1 layered silicates, the lateral dimension of

the octahedral and the two tetrahedral sheets must match as they are connected via a joined anionic layer. While redox reactions in a first approximation are topotactic reactions, the dimension of the octahedral sheet changes with progressing reduction. Different mechanisms for resolving the resultant structural mismatch between the two building blocks interconnected by common oxygen atoms have been proposed (Brigatti et al., 2006; Petit et al., 2023). Apart from bond length alteration (both in the octahedral and in the tetrahedral layer) and tilting/corrugation of the tetrahedral layer out of the (001) plane, the rotation of the tetrahedra perpendicular to the (001) plane and the flattening of the octahedral layer are regarded as the most effective mechanisms. Despite these adjustment mechanisms significant strain will build up during redox reactions. Dioctahedral layered silicates like nontronite or montmorillonite have a more flexible octahedral layer and might behave different from trioctahedral ones like VMT. For instance, when oxidizing ferrous tainiolite, a trioctahedral mica, the local strain becomes too large and instead of a topotactic reaction at some point charge balance with further oxidation is realized by expelling structural octahedral Li^+ into the interlayer space (Mariychuk et al., 2007). In the same line, it is hypothesized that during the reduction of VMT, local stress build-up can no longer be compensated, the redox potential is changed by the stress, and the reduction is brought to a standstill. Validation of this hypothesis would require local structural data, which are difficult, if at all, to access for such a disordered swollen VMT.

4. Conclusions

As shown previously by others, 2:1 layered silicates with high charge densities may successfully and spontaneously be delaminated by complete ion exchange of pristine interlayer cations (predominately Mg^{2+}) with bulky organocations (Daab et al., 2017; Dudko et al., 2022; Walker, 1960). As the divalent Mg^{2+} has a high selectivity for the interlayer space, utter ion exchange is challenging. The equilibrium could, however, be shifted by the complexation of Mg^{2+} by citrate. Successful and utter delamination of a natural VMT into monolayers was confirmed by both, SAXS, proving the nematic liquid crystalline nature of obtained suspensions, and by AFM, confirming monolayers.

As the ratio of edge to external basal surface area changes drastically upon delamination, the material allowed for reinspection of the long-standing dispute of whether electrons can only be injected through edges or whether there is a substantial contribution through basal plane injection. The substantial difference in the maximum degree of reduction suggests that injection through basal planes is indeed substantial. Nevertheless, for reasons not fully understood, reduction is limited to some 50% of structural Fe even for monolayers.

The unique combination of monolayers with a huge aspect ratio that can produce ROS during anoxic/oxic redox cycles in natural compartments renders this filler very promising for polymer nanocomposites. In particular, short-time-use food packaging requires both high barrier and degradability that might be driven by a Fenton type reaction if packaging is unintentionally disposed into the environment. This will help to mitigate microplastic pollution.

Delaminated VMT monolayers thus not only deliver extremely high aspect ratios as required for advanced packaging applications but have potential to accelerate oxidative degradation via ROS generated by redox-cycling. Quite pleasing, delamination of VMT into monolayers optimizes both barrier and ROS production at the same time. Work in this direction is in progress. VMT monolayers will be incorporated into nanocomposites of polymers carrying redox-sensitive functional groups like sulfide.

CRediT authorship contribution statement

Xiong Xiong: Writing – original draft, Validation, Methodology, Investigation, Formal analysis, Data curation. **Felix Uhlig:** Writing – original draft, Investigation, Data curation. **Ingmar Pietsch:** Methodology, Formal analysis. **Nashmiya Basheer:** Investigation, Data curation. **Sabine Rosenfeldt:** Writing – original draft, Investigation, Formal analysis. **Georg Papastavrou:** Writing – review & editing. **Stefan Peiffer:** Writing – review & editing. **Tillmann Lueders:** Writing – review & editing. **Josef Breu:** Writing – review & editing, Supervision, Funding acquisition, Conceptualization.

Declaration of competing interest

The authors declare that they have no known competing financial interests or personal relationships that could have appeared to influence the work reported in this paper.

Appendix A. Supplementary data

Supplementary data to this article can be found online at https://doi.org/10.1016/j.clay.2026.108233.

Data availability

Data will be made available on request.

References

Adelstein, N., Neaton, J.B., Asta, M., De Jonghe, L.C., 2014. Density functional theory based calculation of small-polaron mobility in hematite. Phys. Rev. B 89, 245115. https://doi.org/10.1103/PhysRevB.89.245115.

Babuponnusami, A., Muthukumar, K., 2014. A review on Fenton and improvements to the Fenton process for wastewater treatment. J. Environ. Chem. Eng. 2, 557–572. https://doi.org/10.1016/j.jece.2013.10.011.

Bard, A.J., 2017. Standard Potentials in Aqueous Solution. Routledge.

Barshad, I., 1948. Vermiculite and its relation to biotite as revealed by base exchange reactions, x-ray analyses, differential thermal curves, and water content. Am. Mineral. 33, 655–678.

Barshad, I., Kishk, F.M., 1968. Oxidation of ferrous iron in vermiculite and biotite alters fixation and replaceability of potassium. Science 162, 1401–1402. https://doi.org/10.1126/science.162.3860.1401.

Bergaya, F., Lagaly, G., 2013. Handbook of Clay Science. Newnes.

Brigatti, M.F., Galan, E., Theng, B., 2006. Structures and mineralogy of clay minerals. Develop. Clay Sci. 1, 19–86. https://doi.org/10.1016/S1572-4352(05)01002-0.

Byrne, J.M., Klueglein, N., Pearce, C., Rosso, K.M., Appel, E., Kappler, A., 2015. Redox cycling of Fe(II) and Fe(III) in magnetite by fe-metabolizing bacteria. Science 347, 1473–1476. https://doi.org/10.1126/science.aaa4834.

Celina, M.C., 2013. Review of polymer oxidation and its relationship with materials performance and lifetime prediction. Polym. Degrad. Stab. 98, 2419–2429. https://doi.org/10.1016/j.polymdegradstab. 2013.06.024.

Chen, L., Zhao, Y., Chen, T., Bai, H., Zhang, T., Li, H., An, Q., Song, S., 2019. Correlation of aspect ratio of montmorillonite nanosheets with the colloidal properties in aqueous solutions. Results Phys. 15, 102526. https://doi.org/10.1016/j.rinp.2019.102526.

Chidsey, C.E.D., 1991. Free energy and temperature dependence of electron transfer at the Metal-Electrolyte interface. Science 251, 919–922. https://doi.org/10.1126/science.251.4996.919.

Daab, M., Rosenfeldt, S., Kalo, H., Stöter, M., Bojer, B., Siegel, R., Förster, S., Senker, J., Breu, J., 2017. Two-step delamination of highly charged, vermiculite-like layered silicates via ordered heterostructures. Langmuir 33, 4816–4822. https://doi.org/10.1021/acs.langmuir.7b01008.

Daab, M., Eichstaedt, N.J., Edenharter, A., Rosenfeldt, S., Breu, J., 2018a. Layer charge robust delamination of organo-clays. RSC Adv. 8, 28797–28803. https://doi.org/10.1039/C8RA05318A.

Daab, M., Eichstaedt, N.J., Habel, C., Rosenfeldt, S., Kalo, H., Schießling, H., Förster, S., Breu, J., 2018b. Onset of osmotic swelling in highly charged clay minerals. Langmuir 34, 8215–8222. https://doi.org/10.1021/acs.langmuir.8b00492.

Deer, W.A., FRS, Howie, R.A., Zussman, J., 2013. Vermiculite (Mg,Ca)0.6–0.9(Mg,Fe3+,Al)6.0[(Si,Al)8O20](OH)4.nH2O, An Introduction to the Rock-Forming Minerals. Mineralogical Society of Great Britain and Ireland.

Dudko, V., Timmins, R.L., Khoruzhenko, O., Röhrl, M., Greve, C., Rosenfeldt, S., Tammelin, T., Agarwal, S., Herzig, E.M., Breu, J., 2022. Spontaneous delamination of affordable natural vermiculite as a high barrier filler for biodegradable food packaging. Mater. Adv. 3, 9052. https://doi.org/10.1039/d2ma00734g.

Dyar, M.D., Agresti, D.G., Schaefer, M.W., Grant, C.A., Sklute, E.C., 2006. Mössbauer spectroscopy of earth and planetary materials. Annu. Rev. Earth Planet. Sci. 34, 83–125. https://doi.org/10.1146/annurev.earth.34.031405.125049.

Eckermann, A.L., Feld, D.J., Shaw, J.A., Meade, T.J., 2010. Electrochemistry of redox-active self-assembled monolayers. Coord. Chem. Rev. 254, 1769–1802. https://doi.org/10.1016/j.ccr.2009.12.023.

Falla, W.R., Mulski, M., Cussler, E.L., 1996. Estimating diffusion through flake-filled membranes. J. Membr. Sci. 119, 129–138. https://doi.org/10.1016/0376-7388(96)00106-8.

Feeney, C.A., Goldberg Harris, A., Michele, Farrell, Karim, P., Oree Keisha, R., 2005. Barrier coating of a non-elastomeric polymer and a dispersed layered filler in a liquid carrier and coated articles.
Förster, S., Apostol, L., Bras, W., 2010. Scatter: software for the analysis of nano- and mesoscale small-angle scattering. J. Appl. Crystallogr. 43, 639–646. https://doi.org/10.1107/S0021889810008289.
Fulajtar, E., Agarwal, S., 2024. From thioether to sulfone: Transforming polyester properties for enhanced degradation. ACS Appl. Polym. Mater. 6, 10768–10778. https://doi.org/10.1021/acsapm.4c01911.
Gabriel, J.-C.P., Sanchez, C., Davidson, P., 1996. Observation of nematic Liquid-Crystal textures in aqueous gels of smectite clays. J. Phys. Chem. 100, 11139–11143. https://doi.org/10.1021/jp961088z.
Gao, P., Liu, X., Guo, Z., Tournassat, C., 2023. Acid-Base properties of Cis-Vacant montmorillonite edge surfaces: a combined First-Principles molecular dynamics and surface complexation modeling approach. Environ. Sci. Technol. 57, 1342–1352. https://doi.org/10.1021/acs.est.2c07171.
Gorski, C.A., Aeschbacher, M., Soltermann, D., Voegelin, A., Baeyens, B., Marques Fernandes, M., Hofstetter, T.B., Sander, M., 2012a. Redox properties of structural fe in clay minerals. 1. Electrochemical quantification of Electron-donating and -Accepting capacities of smectites. Environ. Sci. Technol. 46, 9360–9368. https://doi.org/10.1021/es3020138.
Gorski, C.A., Klüpfel, L., Voegelin, A., Sander, M., Hofstetter, T.B., 2012b. Redox properties of structural fe in clay minerals. 2. Electrochemical and spectroscopic characterization of electron transfer irreversibility in ferruginous smectite, SWa-1. Environ. Sci. Technol. 46, 9369–9377. https://doi.org/10.1021/es302014u.
Gorski, C.A., Klüpfel, L.E., Voegelin, A., Sander, M., Hofstetter, T.B., 2013. Redox properties of structural fe in clay minerals: 3. Relationships between smectite redox and structural properties. Environ. Sci. Technol. 47, 13477–13485. https://doi.org/10.1021/es403824x.
Gray, H.B., Winkler, J.R., 2005. Long-range electron transfer. Proc. Natl. Acad. Sci. 102, 3534–3539. https://doi.org/10.1073/pnas.0408029102.
Guebitz, G.M., Cavaco-Paulo, A., 2008. Enzymes go big: Surface hydrolysis and functionalisation of synthetic polymers. Trends Biotechnol. 26, 32–38. https://doi.org/10.1016/j.tibtech.2007.10.003.
Huang, K., Rowe, P., Chi, C., Sreepal, V., Bohn, T., Zhou, K.G., Su, Y., Prestat, E., Pillai, P. B., Cherian, C.T., Michaelides, A., Nair, R.R., 2020. Cation-controlled wetting properties of vermiculite membranes and its promise for fouling resistant oil–water separation. Nat. Commun. 11, 1097. https://doi.org/10.1038/s41467-020-14854-4.
Hunter, R.J., 2013. Zeta potential in colloid science: principles and applications. Academic press.
Hynes, M.J., Kelly, D.F., 1988. The reduction of iron(III) by ascorbic acid. J. Chem. Soc. Chem. Commun. 849–850. https://doi.org/10.1039/C39880000849.
Israelachvili, J.N., 2011. Intermolecular and Surface Forces. Academic press.
Kontoghiorghes, G.J., Kolnagou, A., Kontoghiorghe, C.N., Mourouzidis, L., Timoshnikov, V.A., Polyakov, N.E., 2020. Trying to solve the puzzle of the interaction of ascorbic acid and iron: redox, chelation and therapeutic implications. Medicines (Basel) 7. https://doi.org/10.3390/medicines7080045.
Krempel, Inc., 2023. Electrical Insulation Mica Products. Available at: https://www.krempel.com/en/products/electrical-insulation/mica-products (accessed 16 April 2026).
Khoruzhenko, O., Wagner, D.R., Mangelsen, S., Dulle, M., Förster, S., Rosenfeldt, S., Dudko, V., Ottermann, K., Papastavrou, G., Bensch, W., Breu, J., 2021. Colloidally stable, magnetoresponsive liquid crystals based on clay nanosheets. J. Mater. Chem. C 9, 12732–12740. https://doi.org/10.1039/D1TC02927D.
Kuznetsov, V., Ottermann, K., Helfricht, N., Kunz, D., Loch, P., Kalo, H., Breu, J., Papastavrou, G., 2020. Surface charge density and diffuse layer properties of highly defined 2: 1 layered silicate platelets. Colloid Polym. Sci. 298, 907–920. https://doi.org/10.1007/s00396-020-04673-w.
Kwon, H., Basran, J., Devos, J.M., Suardíaz, R., van der Kamp, M.W., Mulholland, A.J., Schrader, T.E., Ostermann, A., Blakeley, M.P., Moody, P.C.E., Raven, E.L., 2020. Visualizing the protons in a metalloenzyme electron proton transfer pathway. Proc. Natl. Acad. Sci. 117, 6484–6490. https://doi.org/10.1073/pnas.1918936117.
Lagaly, G., 2006. Chapter 5 Colloid Clay Science. In: Bergaya, F., Theng, B.K.G., Lagaly, G. (Eds.), Developments in Clay Science. Elsevier, pp. 141–245.
Latta, D.E., Neumann, A., Premaratne, W.A.P.J., Scherer, M.M., 2017. Fe(II)–Fe(III) electron transfer in a clay mineral with low fe content. ACS Earth Space Chem. 1, 197–208. https://doi.org/10.1021/acsearthspacechem.7b00013.
Lin, Y., Qiao, J., Sun, Y., Dong, H., 2025. The profound review of Fenton process: what's the next step? J. Environ. Sci. 147, 114–130. https://doi.org/10.1016/j.jes.2023.10.005.
Loch, P., Schuchardt, D., Algara-Siller, G., Markus, P., Ottermann, K., Rosenfeldt, S., Lunkenbein, T., Schwieger, W., Papastavrou, G., Breu, J., 2022. Nematic suspension of a microporous layered silicate obtained by forceless spontaneous delamination via repulsive osmotic swelling for casting high-barrier all-inorganic films. Sci. Adv. 8, eabn9084. https://doi.org/10.1126/sciadv.abn9084.
López-García, J.J., Horno, J., Grosse, C., 2011. Poisson–boltzmann description of the electrical double layer including ion size effects. Langmuir 27, 13970–13974. https://doi.org/10.1021/la2025445.
Mähler, J., Persson, I., 2012. A study of the hydration of the alkali metal ions in aqueous solution. Inorg. Chem. 51, 425–438. https://doi.org/10.1021/ic2018693.
Manceau, A., Drits, V.A., Lanson, B., Chateigner, D., Wu, J., Huo, D., Gates, W.P., Stucki, J.W., 2000. Oxidation-reduction mechanism of iron in dioctahedral smectites: II. Crystal chemistry of reduced Garfield nontronite. Am. Mineral. 85, 153–172. https://doi.org/10.2138/am-2000-0115.
Manjanna, J., 2008. Preparation of Fe(II)-montmorillonite by reduction of Fe(III)-montmorillonite with ascorbic acid. Appl. Clay Sci. 42, 32–38. https://doi.org/10.1016/j.clay.2008.02.005.
Marcus, Y., 1987. The thermodynamics of solvation of ions. Part 2.—the enthalpy of hydration at 298.15 k. J. Chem. Soc. Faaraday Transac. 1: Phys. Chem. Condensed Phas 83, 339–349. https://doi.org/10.1039/F19878300339.
Marcus, Y., 1991. Thermodynamics of solvation of ions. Part 5.—Gibbs free energy of hydration at 298.15 k. J. Chem. Soc. Faraday Trans. 87, 2995–2999. https://doi.org/10.1039/FT9918702995.
Marcus, R.A., 1993. Electron transfer reactions in chemistry. Theory and experiment. Rev. Mod. Phys. 65, 599–610. https://doi.org/10.1103/RevModPhys.65.599.
Marcus, R.A., Sutin, N., 1985. Electron transfers in chemistry and biology. Biochimica et biophysica acta (BBA) - reviews on Bioenergetics 811, 265–322. https://doi.org/10.1016/0304-4173(85)90014-X.
Mariychuk, R., Baumgartner, A., Wagner, F.E., Lerf, A., Dubbe, A., Moos, R., Breu, J., 2007. Synthesis, structure, and electric conductivity of ferrous tainiolite and its oxidative conversion into Coarse-Grained swellable smectite. Chem. Mater. 19, 5377–5387. https://doi.org/10.1021/cm0713778.
Maruvada, A., Shubhakar, K., Raghavan, N., Pey, K.L., O'Shea, S.J., 2022. Dielectric breakdown of 2D muscovite mica. Sci. Rep. 12, 14076. https://doi.org/10.1038/s41598-022-18320-7.
Meides, N., Menzel, T., Poetzschner, B., Löder, M.G.J., Mansfeld, U., Strohriegl, P., Altstaedt, V., Senker, J., 2021. Reconstructing the environmental degradation of polystyrene by accelerated weathering. Environ. Sci. Technol. 55, 7930–7938. https://doi.org/10.1021/acs.est.0c07718.
Michot, L.J., Bihannic, I., Maddi, S., Funari, S.S., Baravian, C., Levitz, P., Davidson, P., 2006. Liquid–crystalline aqueous clay suspensions. Proc. Natl. Acad. Sci. 103, 16101–16104. https://doi.org/10.1073/pnas.0605201103.
Moggridge, G.D., Lape, N.K., Yang, C., Cussler, E.L., 2003. Barrier films using flakes and reactive additives. Prog. Org. Coat. 46, 231. https://doi.org/10.1016/S0300-9440(02)00180-7.
Murad, E., 2010. Mossbauer spectroscopy of clays, soils and their mineral constituents. Clay Miner. 45, 413–430. https://doi.org/10.1180/claymin.2010.045.4.413.
Neumann, A., Olson, T.L., Scherer, M.M., 2013. Spectroscopic evidence for Fe(II)–Fe(III) electron transfer at clay mineral edge and basal sites. Environ. Sci. Technol. 47, 6969–6977. https://doi.org/10.1021/es304744v.
O'Brien, R.W., White, L.R., 1978. Electrophoretic mobility of a spherical colloidal particle. J. Chem. Soc. Faraday Transactions 2 74, 1607–1626. https://doi.org/10.1039/F29787401607.
Ortega-Castro, J., Hernández-Haro, N., Dove, M.T., Hernández-Laguna, A., Sainz-Díaz, C. I., 2010. Density functional theory and Monte Carlo study of octahedral cation ordering of Al/Fe/Mg cations in dioctahedral 2: 1 phyllosilicates. Am. Mineral. 95, 209–220. https://doi.org/10.2138/am.2010.3273.
Paineau, E., Bihannic, I., Baravian, C., Philippe, A.-M., Davidson, P., Levitz, P., Funari, S. S., Rochas, C., Michot, L.J., 2011. Aqueous suspensions of natural swelling clay minerals. 1. Structure and electrostatic interactions. Langmuir 27, 5562–5573. https://doi.org/10.1021/la2001255.
Palin, E.J., Dove, M.T., Hernández-Laguna, A., Sainz-Díaz, I., 2004. A computational investigation of the Al/Fe/Mg order-disorder behavior in the dioctahedral sheet of phyllosilicates. Am. Mineral. 89, 164–175. https://doi.org/10.2138/am-2004-0119.
Pentráková, L., Su, K., Pentrák, M., Stucki, J.W., 2013. A review of microbial redox interactions with structural fe in clay minerals. Clay Miner. 48, 543–560. https://doi.org/10.1180/claymin.2013.048.3.10.
Petit, S., Decarreau, A., Grégoire, B., Ferrage, E., 2023. Generalized relationships between the ionic radii of octahedral cations and the b crystallographic parameter of clays and related minerals. Clay Miner. 58, 143–194. https://doi.org/10.1180/clm.2023.20.
Pothanamkandathil, V., Neumann, A., Thompson, A., Gorski, C.A., 2024. Redox properties of structural fe in clay minerals: 4. Reinterpreting redox curves by accounting for electron transfer and structural rearrangement kinetics. Environ. Sci. Technol. 58, 19702–19713. https://doi.org/10.1021/acs.est.4c07835.
Prescher, C., McCammon, C., Dubrovinsky, L., 2012. MossA: a program for analyzing energy-domain mossbauer spectra from conventional and synchrotron sources. J. Appl. Crystallogr. 45, 329–331. https://doi.org/10.1107/S0021889812004979.
Qian, Y., Scheinost, A.C., Grangeon, S., Greneche, J.M., Hoving, A., Bourhis, E., Maubec, N., Churakov, S.V., Fernandes, M.M., 2023. Oxidation state and structure of fe in nontronite: from oxidizing to reducing conditions. ACS Earth Space Chem 7, 1868–1881. https://doi.org/10.1021/acsearthspacechem.3c00136.
Rosso, K.M., Ilton, E.S., 2005. Effects of compositional defects on small polaron hopping in micas. J. Chem. Phys. 122, 244709. https://doi.org/10.1063/1.1943407.
Rothwell, K.A., Pentrak, M.P., Pentrak, L.A., Stucki, J.W., Neumann, A., 2023. Reduction Pathway-Dependent formation of reactive Fe(II) sites in clay minerals. Environ. Sci. Technol. 57, 10231–10241. https://doi.org/10.1021/acs.est.3c01655.
Ruiz-Conde, A., Ruiz-Amil, A., Perez-Rodriguez, J.L., Sánchez-Soto, P.J., 1996. Dehydration–rehydration in magnesium vermiculite: Conversion from two–one and one–two water layer hydration states through the formation of interstratified phases. J. Mater. Chem. 6, 1557–1566. https://doi.org/10.1039/JM9960601557.
Sainz-Díaz, C.I., Cuadros, J., Hernández-Laguna, A., 2001. Analysis of cation distribution in the octahedral sheet of dioctahedral 2: 1 phyllosilicates by using inverse Monte Carlo methods. Phys. Chem. Miner. 28, 445–454. https://doi.org/10.1007/s002690100171.
Sainz-Díaz, C.I., Palin, E.J., Dove, M.T., Hernández-Laguna, A., 2003. Monte Carlo simulations of ordering of al, fe, and mg cations in the octahedral sheet of smectites and illites. Am. Mineral. 88, 1033–1045. https://doi.org/10.2138/am-2003-0712.
Sainz-Diaz, C.I., Palin, E.J., Hernández-Laguna, A., Dove, M.T., 2003. Octahedral cation ordering of illite and smectite. Theoretical exchange potential determination and

Monte Carlo simulations. Phys. Chem. Miner. 30, 382–392. https://doi.org/10.1007/s00269-003-0324-4.
Sajiki, J., Yonekubo, J., 2003. Leaching of bisphenol a (BPA) to seawater from polycarbonate plastic and its degradation by reactive oxygen species. Chemosphere 51, 55–62. https://doi.org/10.1016/S0045-6535(02)00789-0.
Schaefer, M.V., Gorski, C.A., Scherer, M.M., 2011. Spectroscopic evidence for interfacial Fe(II)−Fe(III) electron transfer in a clay mineral. Environ. Sci. Technol. 45, 540–545. https://doi.org/10.1021/es102560m.
Serrano-Lotina, A., Portela, R., Baeza, P., Alcolea-Rodriguez, V., Villarroel, M., Ávila, P., 2023. Zeta potential as a tool for functional materials development. Catal. Today 423, 113862. https://doi.org/10.1016/j.cattod.2022.08.004.
Shokri, A., Fard, M.S., 2022. A critical review in Fenton-like approach for the removal of pollutants in the aqueous environment. Environ. Chall. 7, 100534. https://doi.org/10.1016/j.envc.2022.100534.
Sposito, G., Skipper, N.T., Sutton, R., Park, S.-H., Soper, A.K., Greathouse, J.A., 1999. Surface geochemistry of the clay minerals. Proc. Natl. Acad. Sci. 96, 3358–3364. https://doi.org/10.1073/pnas.96.7.3358.
Stucki, J.W., 2011. A review of the effects of iron redox cycles on smectite properties. Compt. Rendus Geosci. 343, 199–209. https://doi.org/10.1016/j.crte.2010.10.008.
Suzuki, M., Wada, N., Hines, D.R., Whittingham, M.S., 1987. Hydration states and phase transitions in vermiculite intercalation compounds. Phys. Rev. B 36, 2844–2851. https://doi.org/10.1103/PhysRevB.36.2844.
Tersoff, J., Hamann, D.R., 1985. Theory of the scanning tunneling microscope. Phys. Rev. B 31, 805–813. https://doi.org/10.1103/PhysRevB.31.805.
van Olphen, H., 1965. Thermodynamics of interlayer adsorption of water in clays. I.—Sodium vermiculite. J. Colloid Sci. 20, 822–837. https://doi.org/10.1016/0095-8522(65)90055-3.
Vantelon, D., Montarges-Pelletier, E., Michot, L.J., Pelletier, M., Thomas, F., Briois, V., 2003. Iron distribution in the octahedral sheet of dioctahedral smectites. An fe k-edge x-ray absorption spectroscopy study. Phys. Chem. Miner. 30, 44–53. https://doi.org/10.1007/s00269-002-0286-y.
Wagner, B.A., Buettner, G.R., 2023. Stability of aqueous solutions of ascorbate for basic research and for intravenous administration. Adv Redox Res 9. https://doi.org/10.1016/j.arres.2023.100077.
Walker, G.F., 1960. Macroscopic swelling of vermiculite crystals in water. Nature 187, 312–313. https://doi.org/10.1038/187312a0.
Wu, Q., Van Voorhis, T., 2006. Direct calculation of electron transfer parameters through constrained density functional theory. J. Phys. Chem. A 110, 9212–9218. https://doi.org/10.1021/jp061848y.
Yang, Z., Sun, T., Kleindienst, S., Straub, D., Kretzschmar, R., Angenent, L.T., Kappler, A., 2021. A coupled function of biochar as geobattery and geoconductor leads to stimulation of microbial Fe(III) reduction and methanogenesis in a paddy soil enrichment culture. Soil Biol. Biochem. 163, 108446. https://doi.org/10.1016/j.soilbio.2021.108446.
Yu, C., Ji, W., Li, X., Yuan, S., Zhang, P., Pu, S., 2024. Critical role of mineral Fe(IV) formation in low hydroxyl radical yields during Fe(II)-Bearing clay mineral oxygenation. Environ. Sci. Technol. 58, 9669–9678. https://doi.org/10.1021/acs.est.3c09986.
Zhu, X., Fryd, M., Barrero, C., Merali, S., Fecchio, C., Valentine, A.M., Wayland, B.B., 2016. Kinetic-mechanistic studies of p. cepacia lipase catalyzed corona charge selective micelle degradation. J. Mol. Catal. B Enzym. 133, 187–195. https://doi.org/10.1016/j.molcatb.2016.08.013.